Chinese Journal of Chemical Engineering 90 (2026) 106–120

Contents lists available at ScienceDirect

Chinese Journal of Chemical Engineering

journal homepage: www.elsevier.com/locate/CJChE

Full Length Article

Experimental study on hydrogen explosion venting and flame arresting under different metal copper foam structures

Tao Wang [1, 3, 4, *], Wentao Jiang [1], Yuhuai Sheng [1, *], Shangyong Zhou [1], Fanyi Meng [1], Zhenmin Luo [1, 2, 4]

[1] School of Safety Science and Engineering, Xi'an University of Science and Technology, Xi'an 710054, China
[2] Xi'an Key Laboratory of Urban Public Safety and Fire Rescue, Xi'an 710054, China
[3] Shaanxi Key Laboratory of Prevention and Control of Coal Fire, Xi'an 710054, China
[4] Shaanxi Engineering Research Center for Industrial Process Safety & Emergency Rescue, Xi'an 710054, China

ARTICLE INFO

Article history:
Received 11 August 2025
Received in revised form
15 September 2025
Accepted 16 September 2025
Available online 30 October 2025

Keywords:
Metal copper foam
Hydrogen
Explosion venting
Flame-arresting
Numerical simulation

ABSTRACT

The safe transportation of hydrogen is significantly challenged by its inherent flammability and explosivity. Mitigating explosion risks in hydrogen pipelines constitutes the primary objective of this work. Utilizing an experimental platform for explosion venting and flame-arresting, hydrogen explosion experiments were conducted to examine the influence of venting pressure, pores per inch (PPI), porosity, and copper foam thickness on peak explosion pressure and flame-arresting performance within a pipeline. Fluent numerical simulations were employed to validate structural differences in flame-arresting materials, and the flame-arresting mechanism was analyzed in conjunction with flow field characteristics. The results indicate that as the venting pressure increases, the amount of unburned gas entering the pipeline from the container decreases, causing the secondary pressure peak to disappear and reducing the difficulty of flame arresting. The failure mechanism of 20 mm thick copper foam flame-arresting is divided into two types: the heat removal rate of the flame-arresting material and the collision consumption of active free radicals are insufficient to force the flame to quench (20 PPI $\mathcal{E} = 96\%$) and the copper foam is damaged by the pressure wave in the pipeline, resulting in its loss of flame-arresting (60 PPI $\mathcal{E} = 96\%$). On the premise that the flame-arresting is successful, the larger the PPI, porosity, and thickness, the larger the inner cavity of the copper foam, which will enhance the pressure hindering and absorption effect, which will help the pipeline flame-arresting. This research elucidates the flame-arresting mechanism under pressure wave flame coupling, providing a foundational theory for the explosion venting design of industrial hydrogen storage containers.

1. Introduction

Alongside rapid industrial development and the ongoing optimization of the worldwide energy mix, clean-energy demand, particularly, is rising significantly [1–3]. Hydrogen is hailed as the "clean energy of the 21st century" due to its high calorific value, low pollution, high efficiency, and clean-burning nature, making it a focus of widespread attention [4]. But at the same time, hydrogen has flammable and explosive characteristics, has a high risk of leakage, and has a wide explosion limit range, low minimum ignition energy, and fast flame propagation [5,6]. It also brings significant safety risks. With the expansion of hydrogen energy applications, the risk of related explosion accidents is increasing [7]. During transportation, storage, and use, leakage accidents still occur frequently, which can easily cause explosions [8], resulting in large-scale overpressure damage and high-temperature damage [9,10], which poses a significant threat to the surrounding environment and human safety.

During hydrogen storage, hydrogen can exacerbate the risk of tank rupture and explosion due to the combined action of overpressure from an explosion and flame. The main harms of a hydrogen explosion are high explosion pressure and fast flame propagation [11–13]. Scholars have carried out extensive research

* Corresponding authors.
E-mail addresses: christfer@xust.edu.cn (T. Wang), s18536226201@163.com (Y. Sheng).

https://doi.org/10.1016/j.cjche.2025.09.022

on measures to reduce the harm of hydrogen explosions, including explosion suppression technology, explosion venting technology, and explosion-proofing technology [14–16]. Explosion venting is a common safety measure to reduce overpressure and accident impacts, as it controls the release of post-combustion gases from confined spaces *via* dedicated vents for rapid pressure decay, protecting structure integrity and minimizing incident severity [17,18]. Pipeline drain protection design needs to balance drainage efficiency and flame-arresting to prevent secondary explosion chain disasters, but explosion venting involves complex physical-chemical changes—some high-pressure combustible gases may form expanded jet fire, triggering external combustion or explosion [19,20]. Research on its explosion mechanism and control methods is crucial to improve the safety protection level of industrial hydrogen storage containers.

Many scholars have conducted extensive research on the explosion-venting of combustible gases. Lu *et al.* [21] showed that as hydrogen concentration rises from 20% to 60%, P_{max} in the container and drain tube first increases then decreases (peaking at 40%), and pipeline P_{max} is always higher than container P_{max} at the same concentration; this work clarifies how hydrogen concentration affects explosion intensity and container flow field microscopic changes. Wang *et al.* [22] explored the impact of explosion venting area under different hydrogen degrees on the internal and external overpressure of the pipeline. Experimental data reveal a positive correlation between hydrogen concentration and both internal/external overpressures across varied vent areas. Makarov *et al.* [23] added subgrid-scale (SGS) flame diffusion factor based on the large eddy simulation (LES) model to simulate the main phenomenon of increasing the surface area of the spray flame. The model was verified based on Kumar *et al.*'s [24] hydrogen explosion venting experiment, and the findings showed that the simulation results were consistent with the maximum overpressure value and maximum overpressure time measured in the experiment. Wang *et al.* [25] found that during hydrogen explosion venting, the highest pressure peak occurred inside the container. Under fuel-rich conditions, a double pressure peak structure was observed, resulting from the hindering effect of secondary explosions. Gou *et al.* [26] found that the maximum overpressure inside small cylindrical containers peaked at an equivalence ratio of 1.6 during hydrogen explosion venting. Additionally, the difference between the maximum overpressure and the venting pressure was most significant within the equivalence ratio range of $\Phi = 1.0$ to 2.0. Luo *et al.* [27] found that the presence of obstacles significantly reduces the peak overpressure compared to scenarios without obstacles. Additionally, faster membrane rupture occurs with front-side ignition and low hydrogen concentrations, while higher hydrogen concentrations result in greater explosion overpressure. Shao *et al.* [17]conducted a drainage study on the coalbed methane transmission pipeline and found that adding explosion venting ports to the pipeline can effectively reduce parameters such as explosion flame intensity, speed, and overpressure.

Regarding the study of hydrogen flame-arresting, many scholars have studied the influence of metal materials on flame-arresting properties. Zheng *et al.* [28] show that as the metal-foam thickness increases, the flame is progressively attenuated. When the thickness is 100 mm, the explosion venting flame can be completely quenched to reach a flameless explosion venting state. By reducing the combustion speed, the flameless explosion venting efficiency can be effectively improved. Nie *et al.* [29] studied the effects of metal foams and carbon dioxide on explosion venting characteristics, overpressure reduction, and external pressure. It was found that flame-free explosion venting was achieved at 40 mm foam thickness with 25% CO_2 dilution. Cao *et al.* [30] systematically analyzed the impact of pipeline length and bursting pressure on the hydrogen explosion venting process, and found that as the pipeline length increases, the explosion venting efficiency will decrease. Cao *et al.* [31,32] found that wire mesh significantly suppresses the spread of synthesis-gas explosion flames, and its suppression efficiency depends on the wire mesh structure. P_{max} decreases significantly as both the quantity of wire meshes and their layering increase. Wang *et al.* [33] found that wire mesh exerts a significant inhibitory effect on jet fire. With additional wire-mesh layers added, the flame propagation velocity and overpressure are markedly reduced. Zhou *et al.* [34] discovered through the experiment of exploring the hydrogen explosion venting in the pipeline, and found that the closer the ignition position is to the explosion venting port, the explosion venting effect is significant. Through multi-stage pressure relief and increasing the number of explosion venting ports, hydrogen's explosive intensity in the pipeline can be effectively reduced.

The above research shows that in the hydrogen explosion venting–flame arresting process, the hydrogen concentration and equivalent ratio are the key influencing factors affecting the intensity of the explosion, and changes in the explosion venting conditions can affect the peak of the explosion overpressure. Metal porous materials are effective carriers for hydrogen flame-arresting, and their performance increases with the increase of thickness and number of layers. To effectively explore the influence of metal materials on the flame-arresting performance and explosion venting efficiency of the pipeline. Based on hydrogen explosion venting, this work further added metal copper foam flame-arresting materials and protection against a self-built visual pipeline. Based on the scholars of Sheng *et al.* [35], The explosion venting diameter was 50 mm; compared with the influence of three different specifications of copper foam parameters, including PPI and porosity, copper foam thickness, and explosion venting pressure on explosion venting efficiency and flame-arresting, combined with modified polyethylene explosion venting membrane materials, the impact of hydrogen explosion overpressure on pipeline and material flame-arresting performance. To enhance the efficiency of explosion venting, thereby ensuring the safety and stability of industrial hydrogen storage containers, and providing technical support and scientific basis for the safety protection of storage tanks.

2. Experimental

2.1. Experimental system

A visual pipeline was built based on a 20 L spherical explosion tank to carry out hydrogen explosion venting–flame arresting experiments, illustrated in Fig. 1. The main body is a 20 L spherical tank and visual pipeline (140 mm × 140 mm × 850 mm). The explosion venting apparatus is located between the hollow cylinder at the right end of the visualization pipeline and the explosion ball tank. It consists of an upper and lower clamp and an explosion venting membrane. The hollow cylinder connector has an internal diameter of 110 mm and an external diameter of 130 mm, and a length of 150 mm. The high-speed camera is located at the front of the visualization pipeline to collect flame image information. There are 3 pressure sensors in total. Sensor P_1 is located on the side of the spherical tank for collecting pressure data in the spherical tank. Sensors P_2 and P_3 are located at the bottom of the pipeline, 350 mm and 1000 mm from the left side of the tank, respectively, and are used to collect pressure parameters of the front and rear ends of the flame-arresting material in the pipeline. The ignition electrode was centrally positioned within the spherical explosion vessel, using 3.5 J of ignition energy.

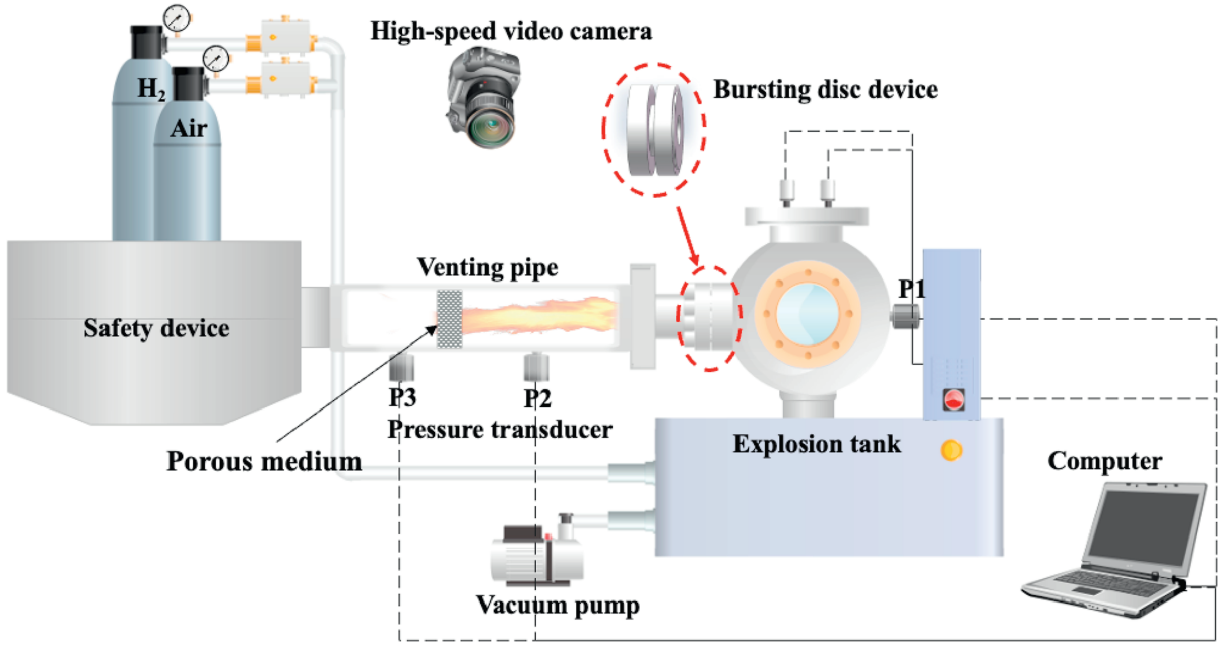

Fig. 1. Schematic diagram of explosion venting–flame arresting experimental platform.

Before each experiment started, the explosion venting membrane material was installed between the upper and lower clamps, and the metal copper foam flame-arresting was placed at 300 mm from the explosion venting port in the pipeline. After vacuuming, premixed hydrogen was introduced to the target concentration. the hydrogen–air mixture was arranged in the explosion tank *via* the method of partial pressures, and the hydrogen–air premixed gas was left to premix for 300 s before igniting. Start the synchronous trigger system, and high-speed cameras and three pressure sensors simultaneously record the flame shape and pressure evolution. Each experimental was repeated three times, and the mean value was used for analysis. After the experiment was completed, the residual gas was replaced, the flame-arresting material and the explosion venting membrane were replaced, and the steps above were repeated.

2.2. Materials and test scenarios

The flame-arresting material was selected for the metal copper foam. Because of its strong thermal conductivity and efficient flame-arresting properties, three specifications were selected: 20 PPI $\mathcal{E} = 80\%$, 20 PPI $\mathcal{E} = 96\%$ and 60 PPI $\mathcal{E} = 96\%$, as shown in Fig. 2.

The impact of copper foam parameters (PPI, porosity), explosion venting pressure, and hydrogen equivalent ratio on the explosion venting protection efficiency of the container is explored. The experimental conditions are shown in Table 1.

2.3. Analysis of hydrogen explosion venting pressure parameters

The explosion parameters are defined as shown in Fig. 3. Fig. 3 (a) is the hydrogen explosion pressure curve, and Fig. 3(b) is the static operation pressure of the hydrogen explosion. The peak explosion pressure of hydrogen is defined as P_{max}, and the maximum peak pressure of hydrogen is the largest in the case of an equivalent ratio of 1. As shown in Fig. 3(b). On the P_1 pressure curve, P_{max11} and P_{max12} denote the first and second pressure maxima, respectively. P_{max21}, P_{max22}, P_{max31}, and P_{max32} are defined in similar ways.

3. Results and Discussion

3.1. Analysis of hydrogen explosion venting– flame arresting pressure

3.1.1. Analysis of pressure propagation characteristics

Fig. 4 (a) shows the pressure changes in the container and pipeline under different equivalent ratios when $P_{stat} = 0.105$ MPa, and under pure explosion venting conditions without adding copper foam flame-arresting material. When $\Phi = 0.6$, P_1 only has one pressure peak value of P_{max11}, due to insufficient unburned gas entering the pipeline under fuel-lean conditions to initiate secondary explosion. When $\Phi = 1.0$ and 1.4, after the explosion discharge membrane is opened, the unburned gas enters the pipeline and mixes with the air in the pipeline, and then the high-speed oscillating flame enters the pipeline, igniting the gas mixture in the channel, resulting in a secondary explosion in the pipeline and forming a bimodal structure.

Fig. 4 (b) shows the pressure change in the container and pipeline under different equivalent ratios after adding copper foam flame-arresting material when $P_{stat} = 0.105$ MPa. Compared with Fig. 4 (a), pure explosion venting of metal copper foam, the pressure curves in the figure lack the second pressure peak caused by the secondary explosion. Over time, only one pressure peak occurs in P_1, P_2, and P_3 under different equivalent ratio conditions. This is because the presence of the flame-arresting material causes the pressure wave to reflect into the container in advance, preventing the unburned gas from continuing to move into the pipeline, thereby effectively suppressing the occurrence of secondary explosions [36]. Compared with the pressure curve in Fig. 4 (a), the pressure of P_2 is smoother, and the peak increases due to the reduction of the explosion venting efficiency of the copper foam.

3.1.2. Analysis of hydrogen explosion venting-flame arresting pressure evolution

Fig. 5 shows the pressure evolution trend of 20 PPI $\mathcal{E} = 80\%$ copper foam with a thickness of 40 mm as a flame-arresting when

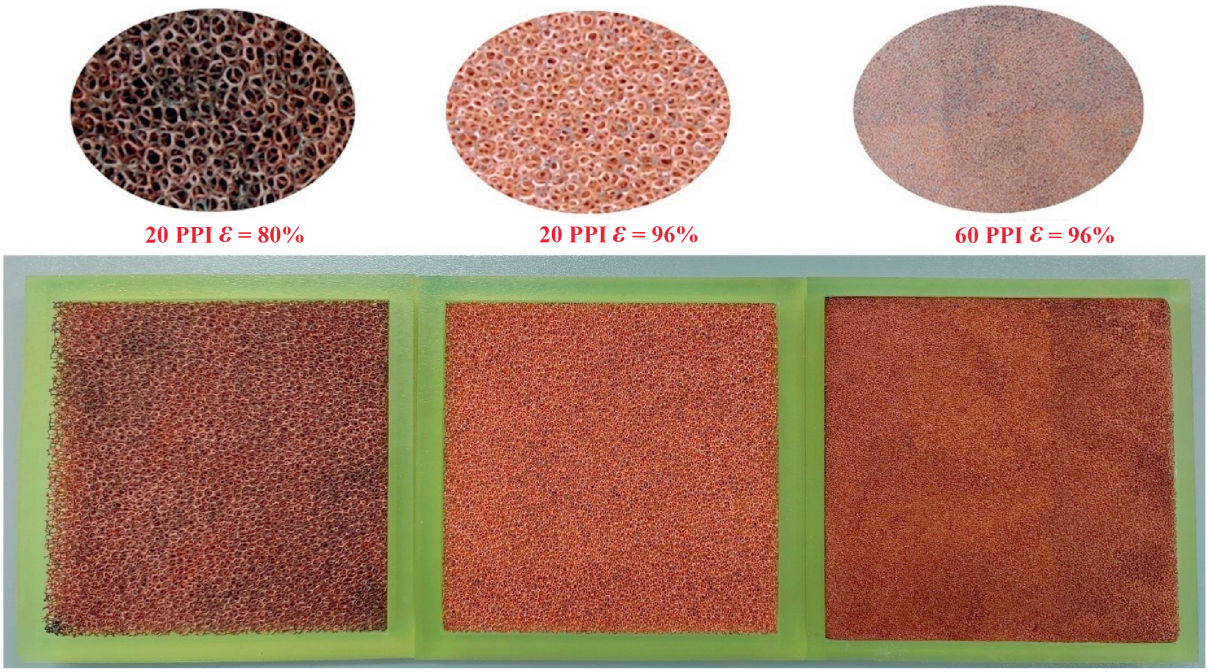

Fig. 2. Actual drawing of metal copper foam.

Table 1
Explosion venting–flame arresting experiment condition.

Cope foam model	Hydrogen equivalent ratio	Venting diameters/mm	Venting stress/MPa
20 PPI $\mathcal{E}=80\%$	0.6	50	0.07\0.105\0.14\0.175
20 PPI $\mathcal{E}=80\%$	1.0	50	0.07\0.105\0.14\0.175
20 PPI $\mathcal{E}=80\%$	1.4	50	0.07\0.105\0.14\0.175
20 PPI $\mathcal{E}=96\%$	0.6	50	0.07\0.105\0.14\0.175
20 PPI $\mathcal{E}=96\%$	1.0	50	0.07\0.105\0.14\0.175
20 PPI $\mathcal{E}=96\%$	1.4	50	0.07\0.105\0.14\0.175
60 PPI $\mathcal{E}=96\%$	0.6	50	0.07\0.105\0.14\0.175
60 PPI $\mathcal{E}=96\%$	1.0	50	0.07\0.105\0.14\0.175
60 PPI $\mathcal{E}=96\%$	1.4	50	0.07\0.105\0.14\0.175

$\Phi=1.4$. As the P_{stat} value increases, P_{max11} and P_{max21} rose slightly by 1.15% and 1.4%, respectively. Because the higher P_{stat} value delays the opening time of the explosion venting plate, allowing more unburned gas to stay in the container, extended residence of unburned gas within the vessel intensifies and completes the combustion reaction, and more heat is released, thereby increasing the peak pressure of P_{max11} and P_{max21}.

3.1.3. Analysis on the impact of characteristic parameters of copper foam on hydrogen flame arresting pressure

Fig. 6 shows that at $\Phi=1.0$ and P_{stat} of 0.105 MPa, both 20 PPI $\mathcal{E}=96\%$ and 60 PPI $\mathcal{E}=96\%$ copper foam fail, but the failure mechanisms are different. Compared with 20 PPI $\mathcal{E}=96\%$, P_{max11} and P_{max21} of 60 PPI $\mathcal{E}=96\%$ copper foam rose by 1.65% and 5.68% respectively, and P_{max31} rose by 2.28%. Since the higher the PPI

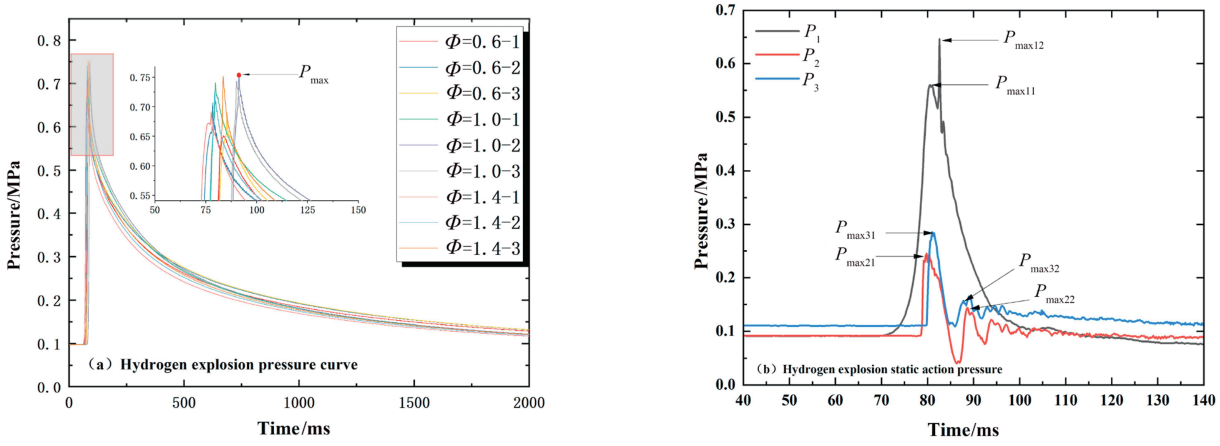

Fig. 3. Diagram of the definition of explosion venting–flame arresting parameters.

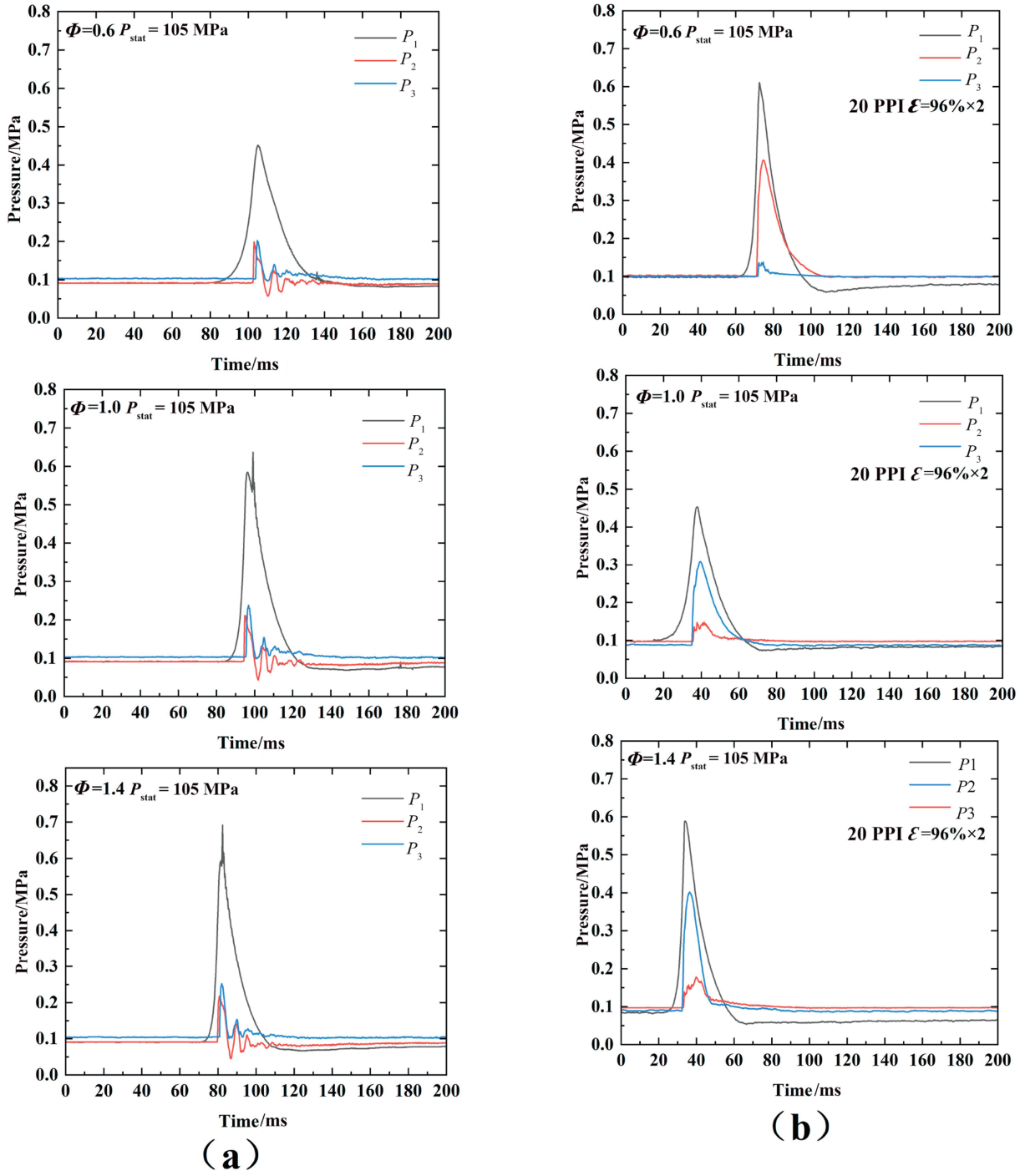

Fig. 4. Evolution in the explosion venting pressure curve of different equivalent ratios.

value, the pressure at the front and rear ends of the copper foam is increased, and the pressure wave reflects strongly at the front end of the copper foam. The increase in PPI also makes the copper foam channel narrower, allowing the flame to continue spreading through the damaged copper foam. This is similar to Zheng *et al.* [37] 's conclusion, increasing PPI leads to an increase in flame velocity and overpressure, and makes the downstream flame more irregular.

Fig. 7 shows the downforce trend of 40 mm thick copper foam 20 PPI $\mathcal{E} = 80\%$ and 20 PPI $\mathcal{E} = 96\%$ as the ignition resist material under $\Phi = 1.4$ and $P_{stat} = 0.105$ MPa. P_{max31} using 20 PPI $\mathcal{E} = 96\%$ copper foam reduces the pressure by 12.74% compared with 20 PPI $\mathcal{E} = 80\%$ copper foam. It shows that P_{max31} is higher due to the failure of flame-arresting of 20 PPI $\mathcal{E} = 80\%$ copper foam, while P_{max31} is lower due to the success of flame-arresting of 20 PPI $\mathcal{E} = 96\%$ copper foam.

High porosity ($\mathcal{E} = 96\%$) copper foam leads to an increase in front-end pressure (P_1) due to its larger internal cavity and enhanced reflection. At the same time, its complex pore path significantly extends the pressure wave propagation time, and

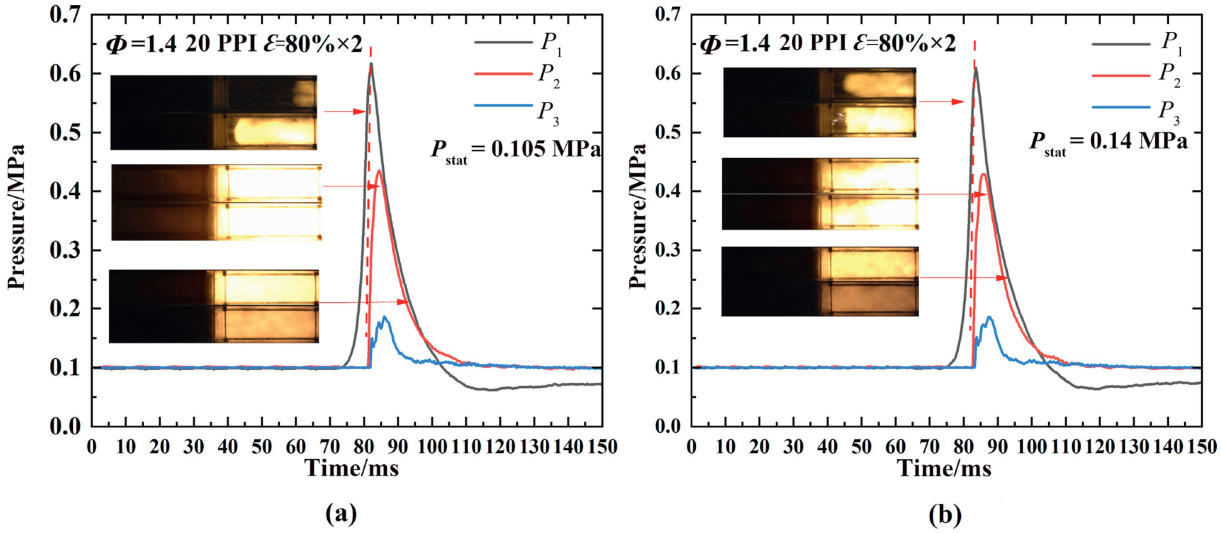

Fig. 5. Evolution in copper foam flame-arresting pressure under different explosion venting pressures.

absorbs energy through turbulent dissipation and heat loss, so that the back-end pressure is rapidly attenuated. On the contrary, the larger pores in low-porosity ($\mathcal{E}$ = 80%) materials cause the peak pressure to reach the rear end earlier, increasing the risk of overpressure.

Fig. 8 shows that 20 mm flame-arresting experiments and 40 mm flame-arresting experiments were performed using 20 PPI $\mathcal{E}$ = 96% copper foam under Φ = 1.0 and P_{stat} = 0.105 MPa. From the figure, the 40 mm copper foam flame-arresting is successful, while the 20 mm copper foam flame-arresting fails. Compared with P_{max31}, it was found that the peak pressure of using 40 mm copper foam flame-arresting is significantly lower than the peak pressure of 20 mm copper foam flame-arresting, the peak pressure decreased by 18.75%.

The 20 mm copper foam exhibits inadequate structural integrity under detonation pressures, undergoing compressive failure that compromises flame-arresting capability. Pressure wave penetration of damaged copper foam results in a significant increase in the back-end pressure (P_{max31}). The 40 mm copper foam enhances energy absorption by extending the pressure wave path, increasing the front-end pressure P_{max21} and a decrease of the rear-end pressure P_{max31} [38]. The multi-layer structure aggravates the reflection and enhances the turbulent intensity in the container [39], making the pressure peak of P_{max11} higher than 20 mm.

3.2. Analysis of the propagation characteristics of hydrogen explosion venting-flame arresting

3.2.1. Analysis of flame under different explosion-venting pressures

When Φ = 1.4, Fig. 9 shows the flame evolution of copper foam as the flame arresting material when P_{stat} = 0.105 MPa and P_{stat} = 0.14 MPa. Experimental observations demonstrate that flame evolution within the pipeline closely resembles sealed-pipeline propagation characteristics following installation of the flame-arresting material. The flame undergoes “hemispherical”, “fingertip” shape, “planar” and “tulip-shaped” shapes before contacting the flame-arresting material, which shows that the flame-arresting material plays a similar role in sealing. Through in-depth analysis of the spatiotemporal development of the flame

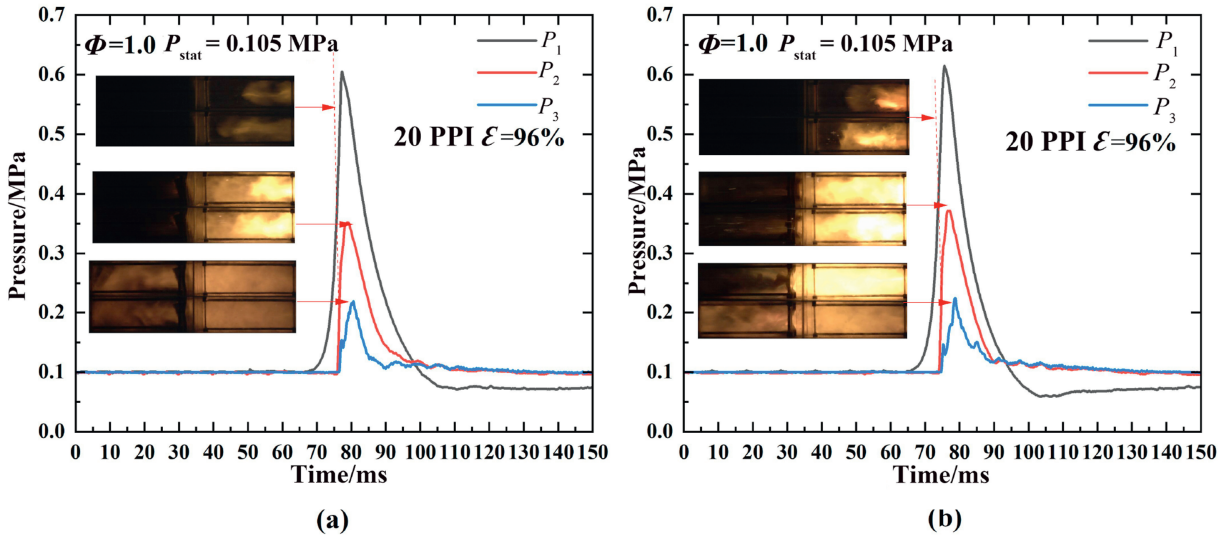

Fig. 6. Evolution in copper foam flame-arresting pressure of different PPI.

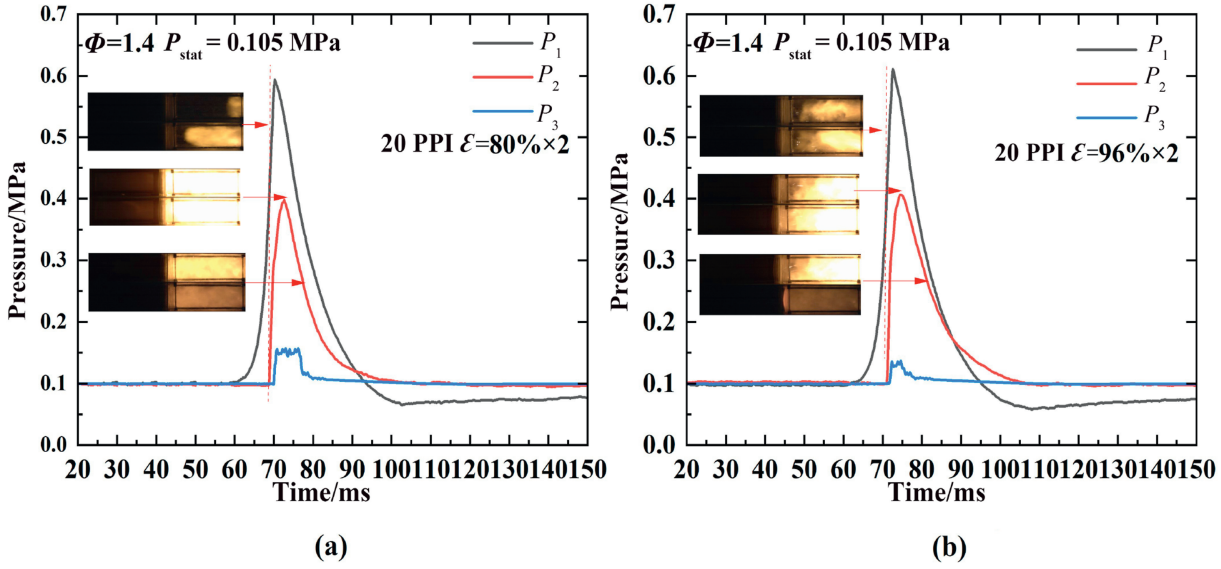

Fig. 7. Evolution in copper foam flame-arresting pressure under different porosities.

morphology in the pipeline, the coupling propagation mechanism between premixed combustion and pressure waves can be revealed. During this process, the formation of the “tulip [40]" flame will significantly increase the thermal stress on the tube wall.

When P_{stat} = 0.14 MPa, the blasting membrane opens later, and less unburned gas is released. The turbulent action of copper foam causes the flame to appear unstable and fragmented, with a multi-branched form. The “tulip-shaped” flame formed in the later stage of propagation has a darker brightness, indicating that the flame-arresting material effectively weakens the flame energy through heat loss and turbulent dissipation, and the flame-arresting is successful. When P_{stat} = 0.105 MPa, the blasting membrane is opened in advance, resulting in a substantial volume of unburned gas leaking, and the combustion reaction in the pipeline causes a sharp increase in the local thermal stress of the pipeline wall, resulting in a failure of flame-arresting. This is because the larger the P_{stat}, the later the blasting membrane opens, the less unburned gas is released, and the combustion reaction is easier to suppress due to the reduction of combustible gas.

3.2.2. Analysis on the impact of characteristic parameters of copper foam on flame arresting

Fig. 10 shows the flame evolution process when 20 PPI and 60 PPI (both porosity is $\mathcal{E}$ = 96%) copper foam as the flame arresting material when Φ = 1.0 and P_{stat} = 0.105 MPa. Although both materials failed to resist fire, there were significant differences in their failure mechanisms. When 20 PPI $\mathcal{E}$ = 96% porosity copper foam is used as a flame-arresting material, its failure principle is that the heat removal rate of the flame-arresting material and the collision consumption of active radicals are insufficient to force the flame to quench. 60 PPI $\mathcal{E}$ = 96% porosity. The copper foam is narrow due to the narrow pores, and high-pressure shock waves are prone to structural fatigue and fracture. The failure principle is that the pressure wave in the pipeline damages the flame-arresting material before the flame reaches it, so that the flame can continue to propagate through the damaged parts.

Fig. 11 shows the flame propagation process when 20 PPI $\mathcal{E}$ = 80% and 20 PPI $\mathcal{E}$ = 96% copper foams with thicknesses of 40 mm are used as the flame-arresting material under Φ = 1.0 and P_{stat} = 0.105 MPa. When 20 PPI $\mathcal{E}$ = 80%, the flame penetrates the

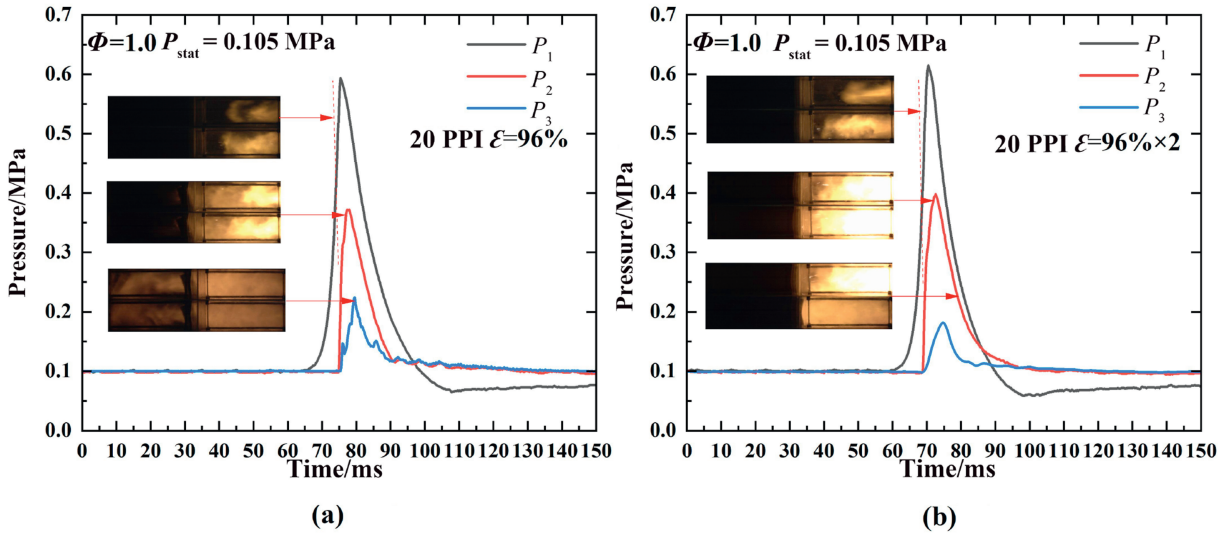

Fig. 8. Evolution in copper foam flame-arresting pressure of different thicknesses.

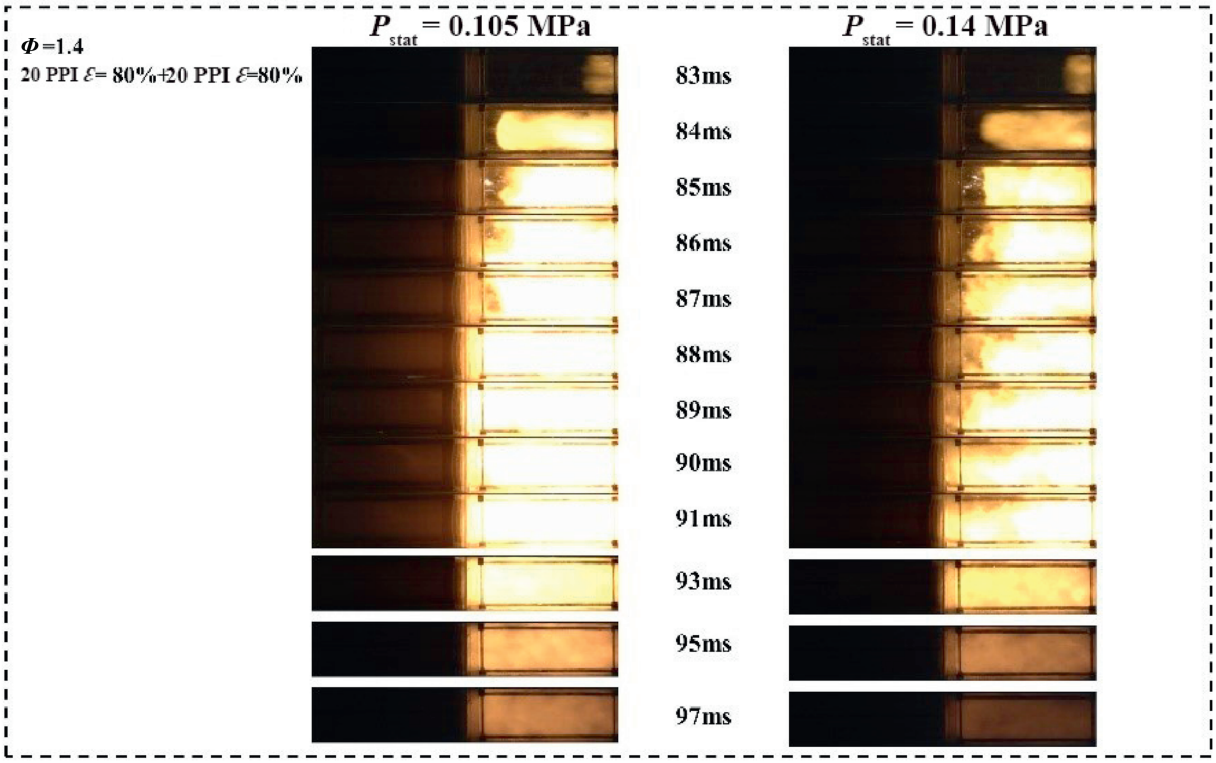

Fig. 9. Diagram of flame evolution under different explosion venting pressures.

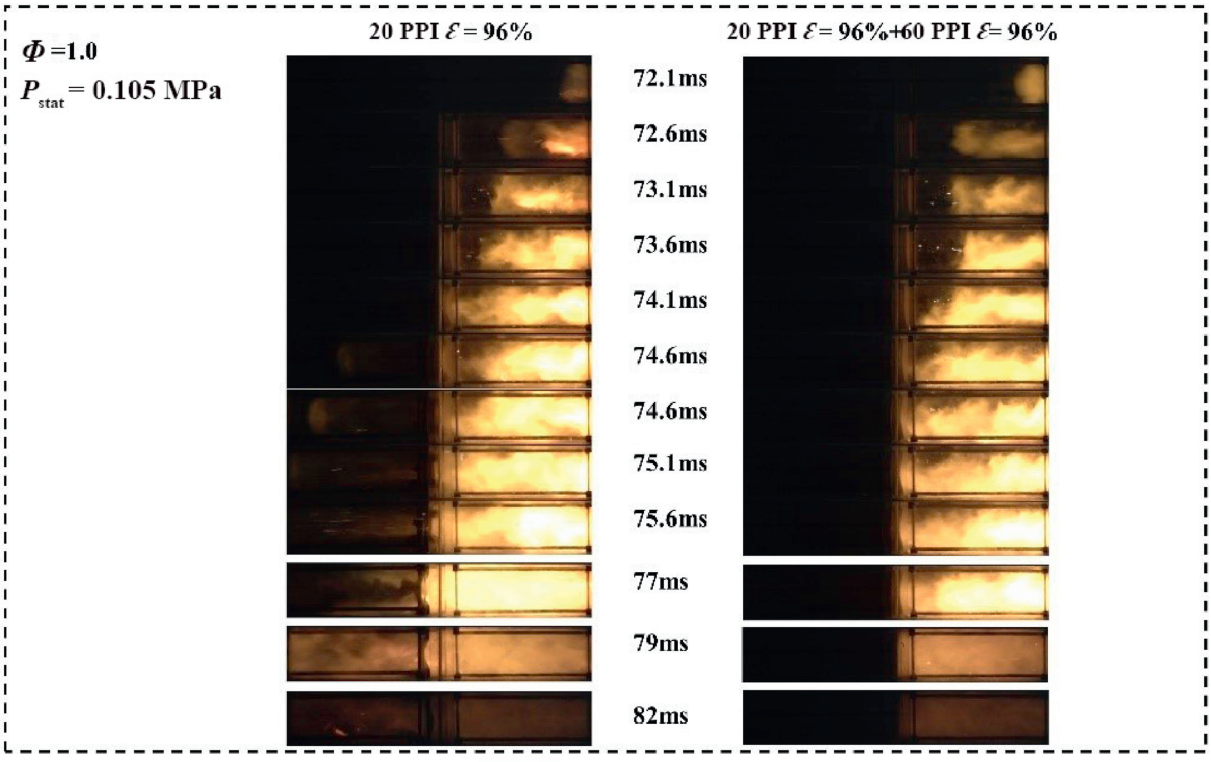

Fig. 10. Diagram of flame evolution under different PPI.

flame-arresting material and causes the flame-arresting to fail, while when 20 PPI $\mathcal{E} = 96\%$, the flame fails to penetrate the flame-arresting material, indicating that the flame-arresting is successful. From the perspective of the flame propagation process [41], the increase in porosity leads to an increase in the volume of the cavity inside the material, and the reflection of the pressure wave at the front end of the material is enhanced, forming a local high-pressure zone, which makes the flame front stay in this area prolong.

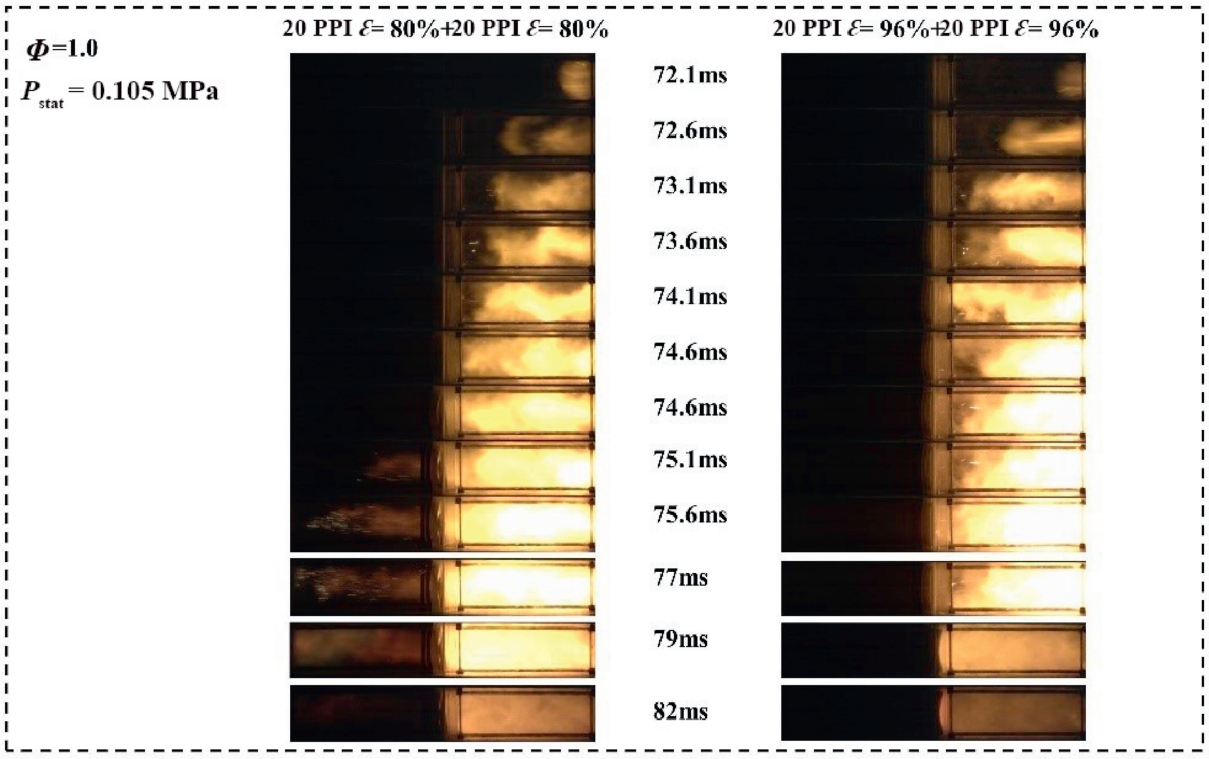

Fig. 11. Diagram of flame evolution under different porosities.

Fig. 12 shows the flame evolution process when (20 mm) 20 PPI $\mathcal{E} = 96\%$ copper foam and (40 mm) 20 PPI $\mathcal{E} = 96\%$ copper foam are used as flame-arresting materials under $\Phi = 1.0$ and $P_{stat} = 0.105$ MPa. When 20 PPI $\mathcal{E} = 96\%$, the flame penetrates the metal copper foam and causes the flame-arresting to fail, The 20 mm-thick copper foam is damaged by the impact of the pressure wave, and the unburned gas undergoes secondary combustion at the back end of the flame-arresting layer, causing the flame

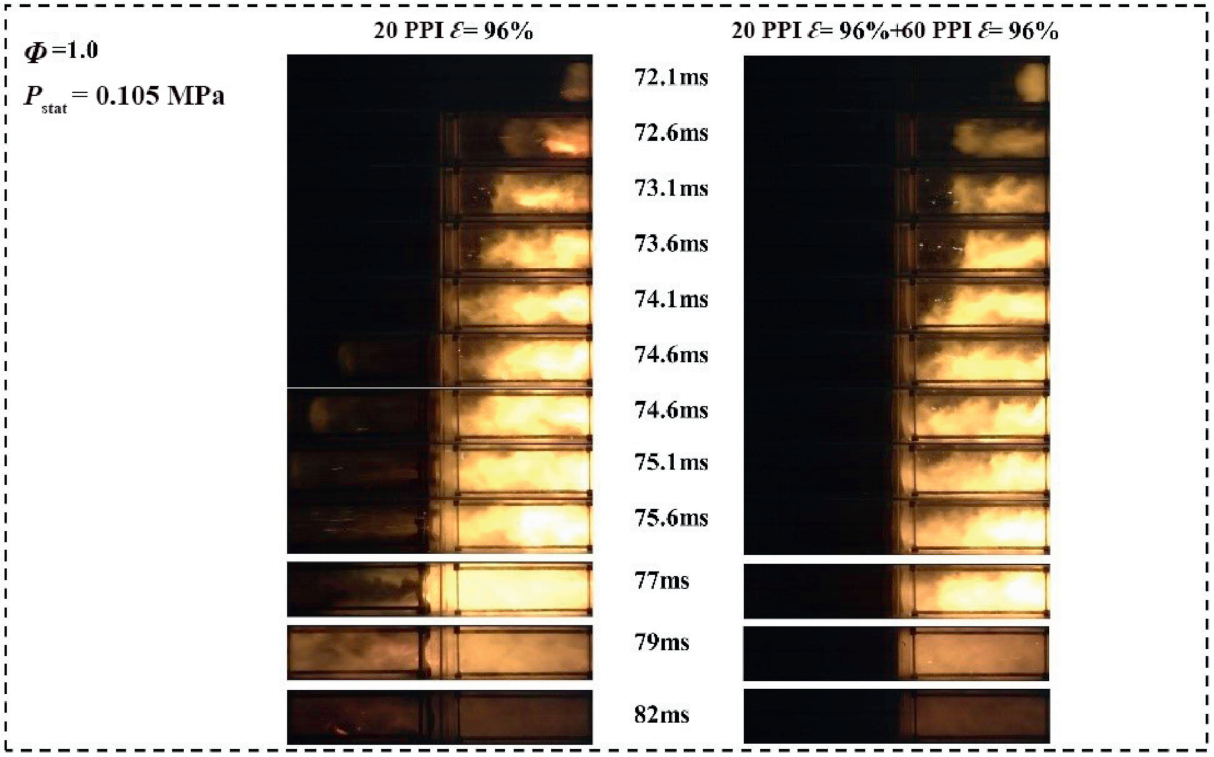

Fig. 12. Diagram of flame evolution under different thicknesses.

to spread rapidly, indicating that the flame breaks through the flame-arresting material and forms an unstable combustion zone. while when (40 mm) 20 PPI $\mathcal{E} = 96\%$, the flame fails to penetrate the flame-arresting material and shows flame-arresting success. The 40 mm copper foam significantly weakens the flame energy and improves the flame-arresting by extending the propagation path and multi-stage reflection.

3.3. Explosion venting—flame arresting numerical simulation and flow field analysis

The hydrogen explosion venting and flame-arresting process involves complex chemical reactions and compressible gas release. Numerical simulations were carried out using Fluent to investigate the flame-arresting mechanism under stoichiometric conditions. A 1:1 two-dimensional model was established based on the experimental setup (Fig. 13), consisting of a spherical vessel with a radius of 0.17 m, two rectangular transition sections (height: 0.11 m, width: 0.15 m), and an irregular hexagonal safety device (length: 1.2 m, height: 0.5 m, outlet width: 0.1 m). Pressure monitoring points were placed at 0.35 m and 1 m from the connection to extract pressure curves for comparison with experimental data from sensors P_2 and P_3. Two layers of copper foam, each 20 mm thick, were incorporated to compare flame-arresting performance between simulation and experiment (see Fig. 14).

At 78 ms, the transmitted pressure wave forms a Mach disk at the constriction structure of the pipeline, causing a sudden increase in local pressure. Under the influence of the reflected wave, the number of Mach disks increases, forming a high-pressure point currently. However, the reverse pressure wave reduces the replenishment of unburned gas into the pipeline, the fuel concentration is lower than the flammable limit, and the secondary explosion conditions are destroyed. Fig. 15 (e) and (E) show the 83 ms moment when the flame did not penetrate the copper foam, and the pressure at the rear end is slightly higher, but the difference is small, indicating that the pressure has dissipated. P_{max32} appeared in the simulation but not in the experiment, because the simulation was the ideal condition, and the energy absorbed by the vibration of the experimental pipeline and the safety device weakened the pressure return. Fig. 15 (g) and (G) show the 88 ms after the point, compared with pure venting, the copper foam

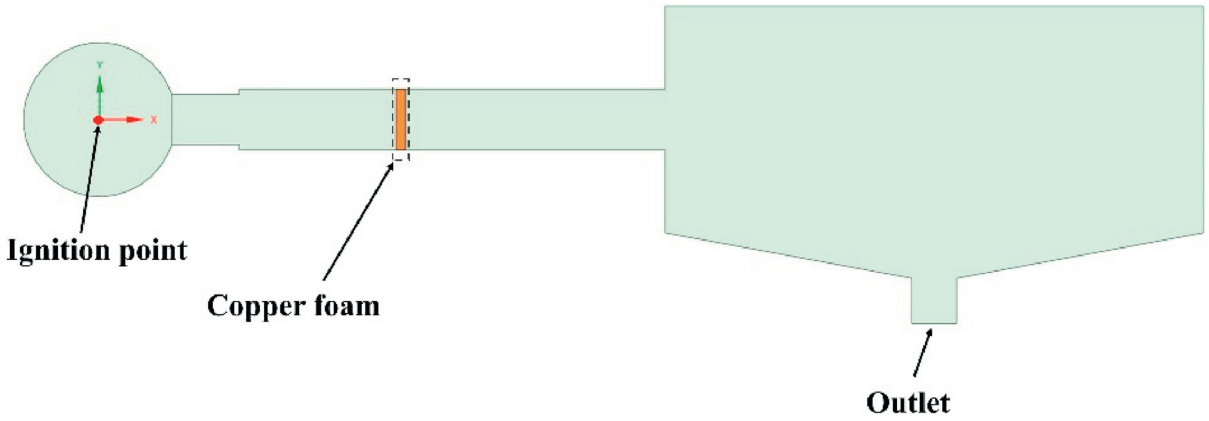

Fig. 13. Numerical simulation calculation model.

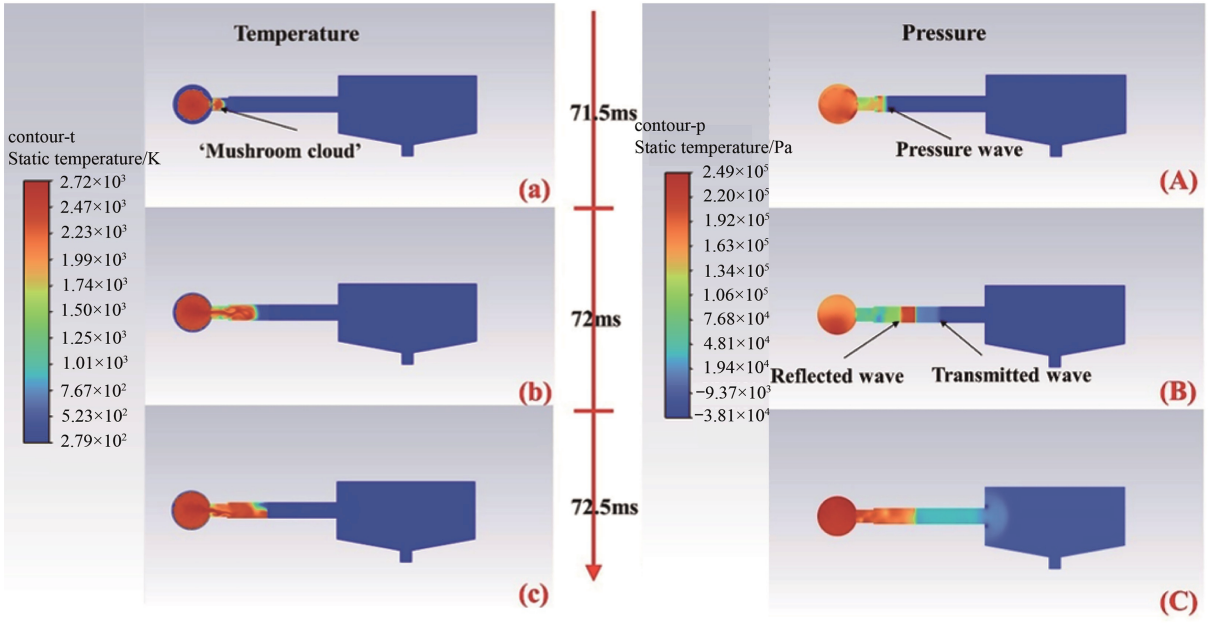

Fig. 14. Contour of downforce propagation and temperature evolution at 60 PPI $\mathcal{E} = 96\%$.

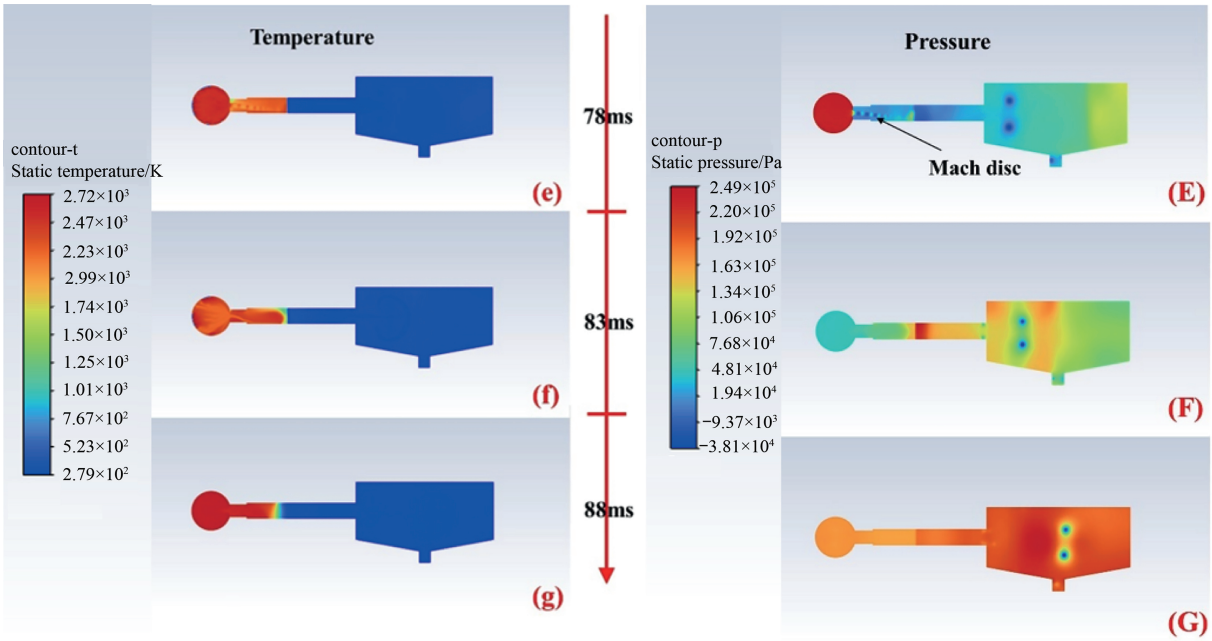

Fig. 15. Downforce propagation and temperature evolution at 60 PPI $\mathcal{E} = 96\%$.

blocks the pressure wave return path, the pressure difference that drives the "residual combustion" cannot be formed in the vessel, and the flame temperature field is completely attenuated. Copper foam cuts off the combustion feedback loop by reflecting the pressure wave and energy dissipation, ensuring that the system is fast and stable.

Fig. 16 shows the flame-arresting effect of using 20 PPI $\mathcal{E} = 96\%$ copper foam during hydrogen explosion venting. At 71.5 ms after ignition, regardless of whether the flame-arresting was successful or not, a typical "mushroom-shaped flame" (red in the core area of high temperature) was formed during the early phase of the hydrogen explosion, and the pressure wave (blue high-value area) propagated rapidly outward. At this time, the copper foam did not significantly affect the flow field, and the flame morphology was consistent with that of pure explosion venting. At 72 ms post-ignition, the high-porosity material ($\mathcal{E} = 96\%$) exhibits inefficient pressure wave reflection, with only partial energy returning toward the container. After the pressure wave of the explosion venting port passes through the copper foam, the reflected wave weakens and the transmitted wave is enhanced, as shown in Fig. 16 (B). The remaining energy quickly penetrates through large pores, propelling the flame forward. As the flame continued to develop and the pressure wave propagated, the flame and pressure wave penetrated the copper foam, as shown in Fig. 16(c) and (C). The

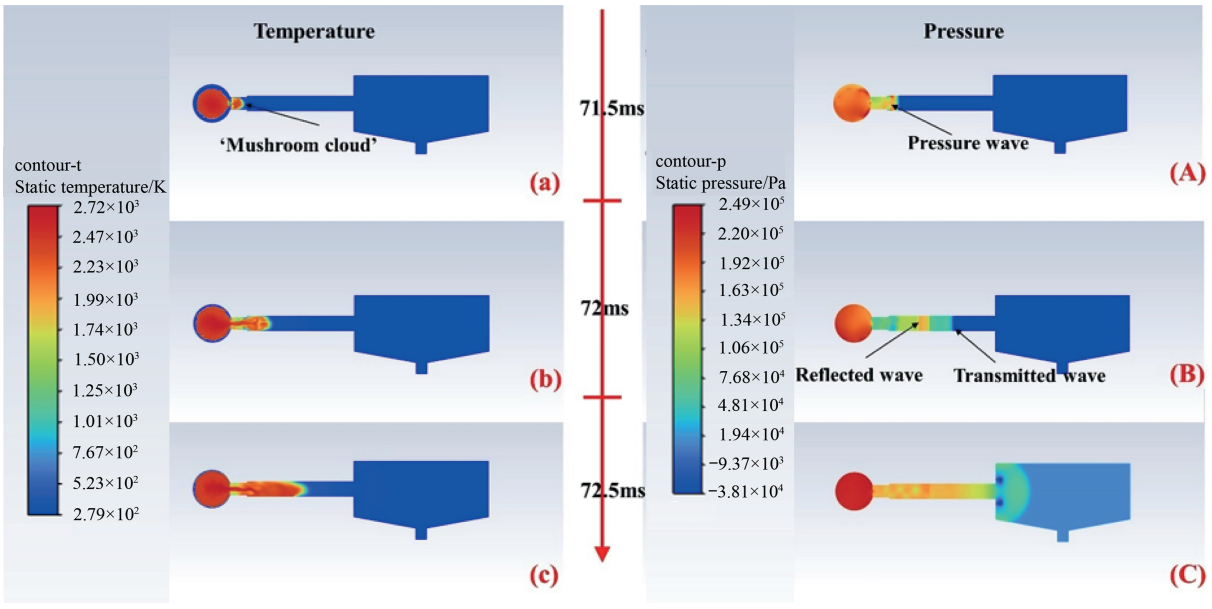

Fig. 16. Contour of downforce propagation and temperature evolution at 20 PPI $\mathcal{E} = 96\%$.

flame front converges toward the central axis more markedly than in pure venting scenarios, primarily attributed to reduced combustible gas diffusion rates and intensified pressure wave projection from the copper foam core, governing flame morphology evolution.

At 78 ms, the front end of the copper foam fails to form a shock wave-induced Mach disk due to the weakening of the reflected pressure wave and its hindrance effect, and the pressure difference disappears. The reflected wave also hinders the inflow of unfueled gas, suppresses the secondary explosion, and temporarily stabilizes the flow field and reduces the flow velocity, thus inhibiting the formation of Mach disks. Fig. 17(e) and (E) show that there is still backflow in the pipeline; however, during the experiment, the vibration of the pipe wall and copper foam weakens the pressure wave, so that the pressure wave is insufficient to trigger backflow in the pipeline. At 83 ms, the damage to the copper foam structure reduces its hindrance efficiency, and the transmitted wave energy is rapidly released at the rear end, accelerating the flame diffusion. With the continuous development of the flame and the continuous propagation of the pressure wave, by 8 ms, although the flame did not cause a secondary explosion, a localized high-temperature region had developed at the rear end, indicating that the combustion was not completely quenched. Flame diffusion is further accelerated, mainly due to reduced copper foam hindrance, which makes it easier for airflow and pressure to propagate to the rear end.

Fig. 18 shows the distribution of the flow field from the initial explosion venting stage of the flame outlet under the condition of 60 PPI $\mathcal{E} = 96\%$. When flames are ejected from the vent, similar to pure explosion venting, vortex rings (Vortex-1) form on both sides of the vent, creating the classic “mushroom cloud” flame form. It's just that due to the decrease in the release pressure, the flame distortion occurs earlier in time, and the “mushroom cloud” flame also appears earlier. As the explosion venting process progresses, it

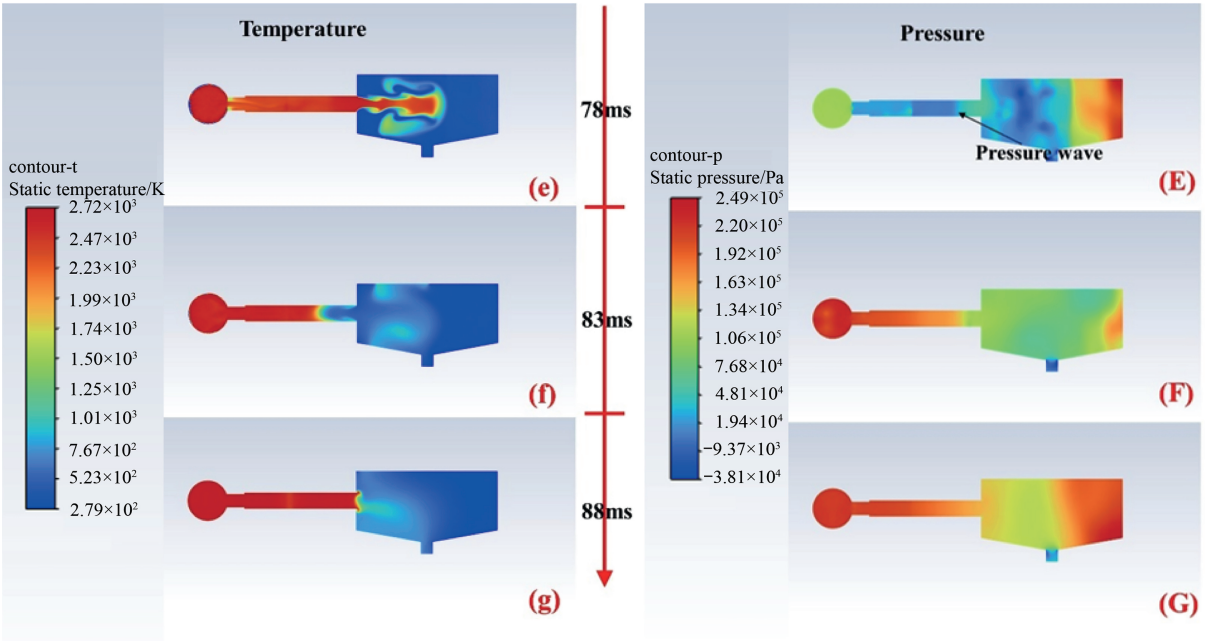

Fig. 17. Contour of 20 PPI $\mathcal{E} = 96\%$ downforce propagation and temperature evolution.

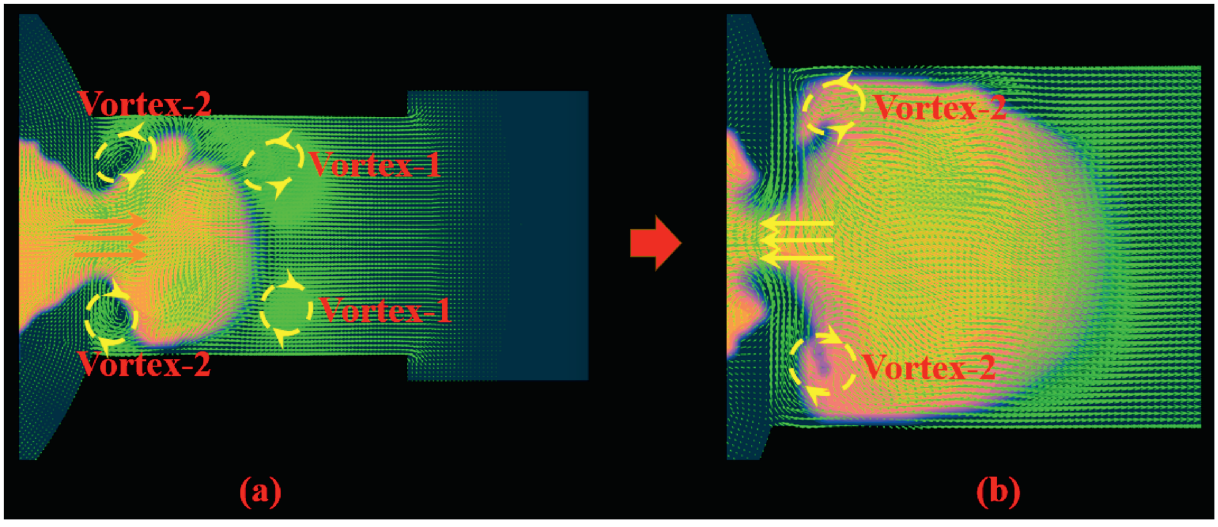

Fig. 18. 60 PPI $\mathcal{E} = 96\%$ downflow field diagram.

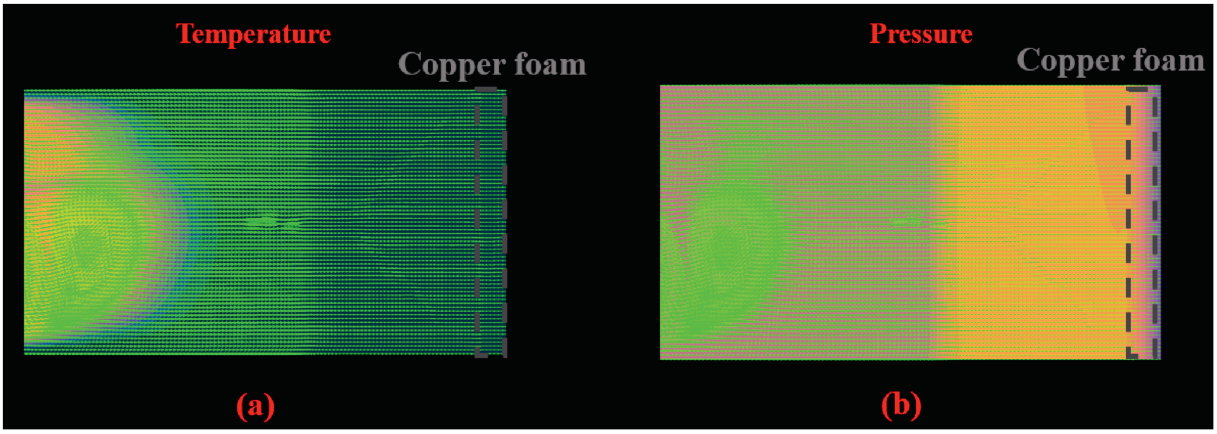

Fig. 19. Flow field diagram of temperature background (a) and pressure background (b) at the same moment at 60 PPI $\mathcal{E} = 96\%$.

can be observed that the released gas has a high flow rate, which plays a leading role in the flame shape. Owing to the wall at the discharge port, the vortex ring "Vortex-1" undergoes lateral stretching, while an additional ring, "Vortex-2," is generated, as illustrated in Fig. 18(a).

Fig. 18(b) shows further changes in flames with a very short return of airflow. This is since the unburned gas enters the pipeline in advance, the flame continues to burn and expand in the pipeline, and the presence of copper foam increases the inertia of the air column in the pipeline, resulting in a brief reflow of the airflow at a certain moment, but this reflux has no significant effect on the pressure in the container. Comparing Fig. 18(a) and (b), it can be clearly seen that the reflected waves generated by copper foam impede the movement of airflow before the flame has propagated to the copper foam position, increasing the value of P_{max21}.

Fig. 19 shows the flow field diagram of the flame reaching copper foam and the flame arresting process at 60 PPI $\mathcal{E} = 96\%$, and the flame front forms a local high-temperature core area when it comes into contact with copper foam, and its diffusion is hindered by the rapid absorption of heat by the highly thermally conductive metal skeleton and inhibits the back-end transfer. At the same time, the high pore density (60 PPI) enhances the reflection of pressure waves, prolongs the propagation time of complex pore paths, and dissipates energy through mixing with turbulence through viscous friction, resulting in a significant attenuation of transmitted pressure. When the pressure reaches its maximum value, there is a gas flow accumulation inside the copper foam, but the flame fails to penetrate the material. This is because the high porosity reflects most of the pressure wave energy, and the remaining energy is weakened by turbulent mixing and viscous dissipation in the pores.

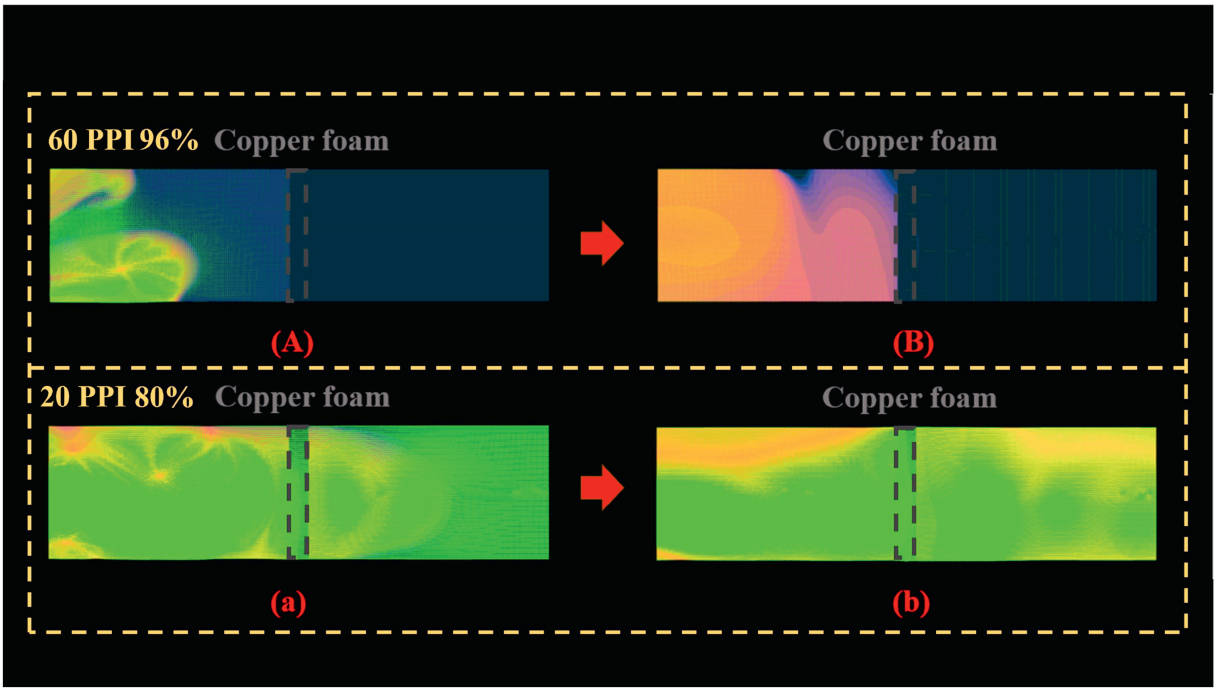

Fig. 20. Flow field diagram of successful and failed flame-arresting.

Fig. 20 shows the flow field characteristics of successful and failed flame-arresting under two different specifications of copper foam. As shown in Fig. 20(A) and (a), the flow field distribution of two specifications of copper foam under the same flame-arresting time, respectively. It can be seen from the figure that under the flame-arresting condition of 60 PPI $\mathcal{E} = 96\%$, the flame development rate is relatively slow, and the flow field behind the copper foam almost disappears. It indicates that the combustible gas and pressure wave cannot penetrate the flame-arresting material, and the flame-arresting was successful. In the case of 20 PPI $\mathcal{E} = 80\%$ copper foam flame-arresting, the flame has completely penetrated the flame-arresting material. Fig. 20(B) and (b) also show the flow field diagram of two specifications of copper foam at the same flame-arresting time, which shows that the flame has completely passed through the flame-arresting material under the flame-arresting state of 20 PPI $\mathcal{E} = 80\%$. The flow field density of the rear end of copper foam is high, which is due to the low porosity ($\mathcal{E} = 80\%$), resulting in a small surface area of the material, and the thermal conductivity is not enough to quench the flame. The sparse pores reduce the compressive ability of the material, and the high-pressure wave causes the pores to collapse and form a penetrating channel.

4. Conclusions

In the present study, the effects of explosion venting pressure, PPI, porosity, and copper foam thickness on the coupling of pressure wave and flame during the hydrogen venting process were explored through the explosion venting flame-arresting experimental system, and the failure mechanism of copper foam flame-arresting success and failure was explored. The structural differences of the flame-arresting materials were verified by numerical simulation, and the flame-arresting mechanism was verified by flow field analysis and the following relevant conclusions were drawn.

(1) The failure principle of 20 PPI $\mathcal{E} = 96\%$ copper foam flame-arresting was that the heat removal rate of the flame-arresting material and the collision consumption of reactive free radicals were not enough to force the flame to extinguish. The failure principle of 60 PPI $\mathcal{E} = 96\%$ copper foam is that the high-pressure wave in the pipeline damages the flame-arresting material before it reaches the flame, so that the flame can continue to propagate through the damaged part.

(2) 40 mm thick copper foam 20 PPI $\mathcal{E} = 96\%$ flame-arresting success, while 20 PPI $\mathcal{E} = 80\%$ flame-arresting failure. It was mainly due to the high front-end pressure and low back-end pressure caused by the higher porosity of copper foam when it was flame-arresting. The greater the effect on the enhancement and absorption of pressure. When the porosity was increased to $\mathcal{E} = 96\%$, the pressure difference between the two ends of the flame-arresting material increases significantly.

(3) Increasing the venting pressure from 0.10 MPa to 0.14 MPa can effectively reduce the leakage of unburnt gas and reduce the intensity of combustion. After the addition of copper foam, the fuel was not enough to support the secondary explosion due to the reduction of the leakage of unburnt gas, so that the peak of the secondary pressure disappears and the peak overpressure of the pipeline (P_{max21}) decreases.

(4) The increase in the thickness of copper foam can improve the success rate of flame-arresting, but its influence on turbulent disturbance in the vessel needs to be considered. 20 PPI $\mathcal{E} = 96\%$ copper foam with a thickness of 20 mm was not strong enough, which will cause damage to the copper foam and the failure of flame-arresting. The 40 mm-thick copper foam has an enhanced inhibitory effect on the pressure wave, so that the flame will be hindered in the early development process and the propagation speed will be slowed down.

(5) The explosion venting was verified and supplemented the field experiment through numerical simulation and flow field analysis, revealing the inhibitory effect of pressure wave reflection and transmission on flame propagation, as well as the blocking effect of fire-retardant materials on “residual combustion”. In the dynamic characteristics of the flow field, high-porosity materials (60 PPI $\mathcal{E} = 96\%$) inhibit the replenishment of unburned gas by weakening the rear-end flow field density; low-porosity materials (20 PPI $\mathcal{E} = 80\%$) accelerated flame penetration due to the concentrated flow field.

CRediT Authorship Contribution Statement

Tao Wang: Funding acquisition, Data curation, Conceptualization. Wentao Jiang: Writing – review & editing, Writing – original draft. Yuhuai Sheng: Methodology. Shangyong Zhou: Formal analysis. Fanyi Meng: Validation. Zhenmin Luo: Resources, Funding acquisition.

Declaration of Competing Interest

The authors declare that they have no known competing financial interests or personal relationships that could have appeared to influence the work reported in this paper.

Acknowledgements

This research was supported by the National Natural Science Foundation of China (52474250 and 52174200).

References

[1] S.P. Guo, Q.B. Liu, J. Sun, H.G. Jin, A review on the utilization of hybrid renewable energy, *Renew. Sustain. Energy Rev.* 91 (2018) 1121–1147.
[2] J.H. Lin, J.M. Sun, Y. Chen, J. Luo, C.W. Cui, S.C. Sun, Valorization of sludge using microwave pyrolysis for green bio-energy: combined effects of key parameters on the directional optimization of high-quality syngas, *Fuel* 326 (2022) 125010.
[3] R.J. Varghese, H. Kolekar, V. Hariharan, S. Kumar, Effect of CO content on laminar burning velocities of syngas-air premixed flames at elevated temperatures, *Fuel* 214 (2018) 144–153.
[4] L. Gong, Q.L. Duan, J.H. Sun, V. Molkov, Similitude analysis and critical conditions for spontaneous ignition of hydrogen release into the atmosphere through a tube, *Fuel* 245 (2019) 413–419.
[5] Y.C. Li, M.S. Bi, B. Li, Y.H. Zhou, W. Gao, Effects of hydrogen and initial pressure on flame characteristics and explosion pressure of methane/hydrogen fuels, *Fuel* 233 (2018) 269–282.
[6] Y.C. Li, M.S. Bi, B. Li, Y.H. Zhou, L. Huang, W. Gao, Explosion hazard evaluation of renewable hydrogen/ammonia/air fuels, *Energy* 159 (2018) 252–263.
[7] Z. Dong, Z.M. Luo, P. Yang, Y.Y. Yu, F.Y. Meng, J. Qu, F.M. Cheng, L.T. Liu, H. Wen, J. Deng, T. Wang, Investigation on the suppression effects of $Na_2CO_3 \cdot 10H_2O$–CO_2 on hydrogen-air deflagration, *Int. J. Hydrogen Energy* 142 (2025) 447–459.
[8] C.D. Lin, X.Y. Cao, Z.R. Wang, J.S. Wei, J.J. Xu, Research on quenching performance and multi-factor influence law of hydrogen crimped-ribbon flame arrester using response surface methodology, *Fuel* 326 (2022) 124911.
[9] M. Balat, E. Kirtay, Major technical barriers to a “hydrogen economy”, *Energy Sources Part A Recovery Util, Environ. Eff.* 32 (9) (2010) 863–876.
[10] J.H. Shi, B. Chang, F. Khan, Y.J. Chang, Y. Zhu, G.M. Chen, C.J. Zhang, Stochastic explosion risk analysis of hydrogen production facilities, *Int. J. Hydrogen Energy* 45 (24) (2020) 13535–13550.
[11] X. Rocourt, S. Awamat, I. Sochet, S. Jallais, Vented hydrogen–air deflagration in a small enclosed volume, *Int. J. Hydrogen Energy* 39 (35) (2014) 20462–20466.
[12] Y. Zhang, R.K. Chen, M.K. Zhao, J.W. Luo, W.S. Feng, W.Q. Fan, Y.X. Tan, W.G. Cao, C.M. Shu, C.J. Yu, Hazard evaluation of explosion venting behaviours for

premixed hydrogen-air fuels with different bursting pressures, *Fuel* 268 (2020) 117313.
[13] B. Zhang, The influence of wall roughness on detonation limits in hydrogen−oxygen mixture, *Combust. Flame* 169 (2016) 333−339.
[14] W.G. Cao, W.J. Li, S. Yu, Y. Zhang, C.M. Shu, Y.F. Liu, J.W. Luo, L.T. Bu, Y.X. Tan, Explosion venting hazards of temperature effects and pressure characteristics for premixed hydrogen-air mixtures in a spherical container, *Fuel* 290 (2021) 120034.
[15] M.D. Gao, M.S. Bi, L.L. Ye, Y.C. Li, H.P. Jiang, M.R. Yang, C.C. Yan, W. Gao, Suppression of hydrogen-air explosions by hydrofluorocarbons, *Process*, *Saf. Environ. Prot.* 145 (2021) 378−387.
[16] P. Yang, T. Wang, Y.H. Sheng, Y.Y. Yu, R.K. Li, B. Su, F.M. Cheng, J. Qu, J. Deng, Z. M. Luo, Recent advances in hydrogen process safety: deflagration behaviors and explosion mitigation strategies, *Process*, *Saf. Environ. Prot.* 188 (2024) 303−316.
[17] H. Shao, S.G. Jiang, Z.Y. Wu, W.Q. Zhang, K. Wang, Application and effect of negative pressure chambers on pipeline explosion venting, *J. Loss Prev. Process. Ind.* 41 (2016) 8−17.
[18] X.H. Jiang, B.C. Fan, J.F. Ye, G. Dong, Experimental investigations on the external pressure during venting, *J. Loss Prev. Process. Ind.* 18 (1) (2005) 21−26.
[19] J. Taveau, Correlations for blast effects from vented dust explosions, *J. Loss Prev. Process. Ind.* 23 (1) (2010) 15−29.
[20] P. Quillatre, O. Vermorel, T. Poinsot, P. Ricoux, Large eddy simulation of vented deflagration, *Ind. Eng. Chem. Res.* 52 (33) (2013) 11414−11423.
[21] Y.W. Lu, R.J. Fan, Z.R. Wang, X.Y. Cao, W.J. Guo, The influence of hydrogen concentration on the characteristic of explosion venting: explosion pressure, venting flame and flow field microstructure, *Energy* 293 (2024) 130562.
[22] Q. Wang, X.J. Luo, C.J. Wang, Y. Liu, P.G. Zhou, B. Li, Experimental study on external explosion for vented hydrogen deflagration in a rectangular tube with different vent coefficients, *Process Saf. Environ. Prot.* 158 (2022) 331−339.
[23] D. Makarov, F. Verbecke, V. Molkov, Numerical analysis of hydrogen deflagration mitigation by venting through a duct, *J. Loss Prev. Process. Ind.* 20 (4−6) (2007) 433−438.
[24] R.K. Kumar, W.A. Dewit, D.R. Greig, Vented explosion of hydrogen-air mixtures in a large volume, *Combust. Sci. Technol.* 66 (4−6) (1989) 251−266.
[25] T. Wang, Y.H. Sheng, F. Nan, L.T. Liu, J. Chen, F.Y. Meng, J. Deng, J.H. Shi, Z.M. Luo, Investigation on the flame and pressure behaviors of vented hydrogen-air deflagration from a duct-connected vessel: effects of venting diameter and static activation pressure, *Energy* 307 (2024) 132705.
[26] J. Guo, X.Y. Liu, C.J. Wang, Experiments on vented hydrogen-air deflagrations: the influence of hydrogen concentration, *J. Loss Prev. Process. Ind.* 48 (2017) 254−259.
[27] X.J. Luo, C.J. Wang, S.C. Rui, Y. Wan, Z. Zhang, Q. Li, Effects of ignition location, obstacles, and vent location on the vented hydrogen-air deflagrations with low vent burst pressure in a 20-foot container, *Fuel* 280 (2020) 118677.
[28] G.J. Zheng, Q.L. Bai, J.F. Cheng, Y.C. Li, W. Gao, Study on hydrogen-air explosion flameless venting with metal foam addition, *Int. J. Hydrogen Energy* 117 (2025) 215−227.
[29] Z.H. Nie, W. Gao, H.P. Jiang, F.Y. Zhao, G.J. Zheng, Z.L. Zhang, Flameless venting characteristics of hydrogen explosion under the coupling of carbon dioxide and metal foam, *Process*, *Saf. Environ. Prot.* 180 (2023) 375−385.
[30] W.G. Cao, Y.F. Liu, R.K. Chen, W.J. Li, Y. Zhang, S. Xu, X. Cao, Q. Huang, Y.X. Tan, Pressure release characteristics of premixed hydrogen-air mixtures in an explosion venting device with a duct, *Int. J. Hydrogen Energy* 46 (12) (2021) 8810−8819.
[31] X.Y. Cao, Z. Wang, Y. Wang, Z.R. Wang, Y.Q. Zhou, Effect of wire mesh structure parameter on the flame propagation characteristics of syngas explosion, *Fuel* 334 (2023) 126658.
[32] Y.W. Lu, Z.R. Wang, X.Y. Cao, Y.Y. Cui, P.P. Sun, C.J. Qian, Interaction mechanism of wire mesh inhibition and ducted venting on methane explosion, *Fuel* 304 (2021) 121343.
[33] Z.R. Wang, Y.W. Lu, X.Y. Cao, Y. Yu, J.C. Jiang, F. Jiao, S.C. Ma, Wire-mesh inhibition of jet fire induced by explosion venting, *J. Loss Prev. Process. Ind.* 70 (2021) 104408.
[34] N. Zhou, P.F. Ni, X. Li, X.W. Li, X.J. Yuan, H.J. Zhao, Experimental study and numerical simulation of the influence of vent conditions on hydrogen explosion characteristics, *Energy Sources Part A Recovery Util*, *Environ. Eff.* 47 (1) (2025) 5771−5786.
[35] Y.H. Sheng, Z.M. Luo, L.T. Liu, Z. Yang, F. Meng, Z. Dong, Y.N. Zhang, J. Qu, J. Deng, T. Wang, Experimental investigation on the vented flame and pressure behaviour of hydrogen-air mixtures, *J. Loss Prev. Process. Ind.* 92 (2024) 105469.
[36] P. Chen, F.J. Huang, Y.D. Sun, X.X. Chen, Effects of metal foam meshes on premixed methane-air flame propagation in the closed duct, *J. Loss Prev. Process. Ind.* 47 (2017) 22−28.
[37] K. Zheng, J.L. Ren, C. Song, Q.H. Jia, Z.Y. Song, Z.X. Xing, Explosion behavior of nonuniform hydrogen/methane/air mixtures in the presence of copper foam, *Fuel* 368 (2024) 131685.
[38] H. Liu, C.H. Wang, M. Li, L.X. Zhou, J.H. Dai, Y.L. Zeng, Y. Li, Structural parameter optimization study of online pipeline flame arresters, *Int. J. Front. Eng. Technol.* 6 (2024).
[39] Y.L. Duan, Z.H. Li, Z.Y. Wen, S.L. Lei, L.L. Zheng, W. Huang, H.L. Jia, Effects of flame arrester core with different thicknesses on hydrogen/methane/air explosion with low hydrogen ratio, *Combust. Sci. Technol.* 196 (18) (2024) 4967−4981.
[40] C.G. Qian, M.A. Liberman, Influence of flame collisions with pressure waves on tulip flame formation and its evolution in tubes with non-slip walls, *Acta Astronaut.* 232 (2025) 154−163.
[41] S.C. Sun, G. Liu, J.X. Liu, C. Ye, J.J. Ren, M.S. Bi, Effect of porosity and element thickness on flame quenching for in-line crimped-ribbon flame arresters, *J. Loss Prev. Process. Ind.* 50 (2017) 221−228.